Electrically Tunable Metal–Semiconductor–Metal Terahertz Metasurface Modulators

Goran Isić ⬤, Georgios Sinatkas ⬤, *Student Member, IEEE*, Dimitrios C. Zografopoulos ⬤, Borislav Vasić, Antonio Ferraro ⬤, *Member, IEEE*, Romeo Beccherelli ⬤, *Member, IEEE*, Emmanouil E. Kriezis ⬤, *Senior Member, IEEE*, and Milivoj Belić ⬤

Abstract—We propose metal–semiconductor–metal cavity arrays as active elements of electrically tunable metasurfaces operating in the terahertz spectrum. Their function is based on reverse biasing the Schottky junction formed between top metal strips and the n-type semiconductor buried beneath. A gate bias between the strips and a back metal reflector controls the electron depletion layer thickness thus tuning the Drude permittivity of the cavity array. Using a rigorous multiphysics framework which combines Maxwell equations for terahertz waves and the drift-diffusion model for describing the carrier behavior in the semiconductor, we find a theoretically infinite extinction ratio, insertion loss of around 10%, and picosecond intrinsic switching times at 1 THz, for a structure designed to enter the critical coupling regime once the depletion layer reaches the bottom metal contact. We also show that the proposed modulation concept can be used for devices operating at the higher end of the terahertz spectrum, discussing the limitations on their performance.

Index Terms—Terahertz metasurfaces, tunable metamaterials.

G. Isić is with the Graphene Laboratory of Center for Solid State Physics and New Materials, Institute of Physics Belgrade, University of Belgrade, Belgrade 11080, Serbia, and also with the Texas A&M University at Qatar, Doha 23874, Qatar (e-mail: isicg@ipb.ac.rs).

G. Sinatkas and E. E. Kriezis are with the School of Electrical and Computer Engineering, Aristotle University of Thessaloniki, Thessaloniki 54124, Greece (e-mail: gsinatka@auth.gr; mkriezis@auth.gr).

D. C. Zografopoulos, A. Ferraro, and R. Beccherelli are with the Consiglio Nazionale delle Ricerche, Istituto per la Microelettronica e Microsistemi, Rome 00133, Italy (e-mail: dimitrios.zografopoulos@artov.imm.cnr.it; antonio.ferraro@artov.imm.cnr.it; romeo.beccherelli@artov.imm.cnr.it).

B. Vasić is with the Graphene Laboratory of Center for Solid State Physics and New Materials, Institute of Physics Belgrade, University of Belgrade, Belgrade 11080, Serbia (e-mail: bvasic@ipb.ac.rs).

M. Belić is with the Texas A&M University at Qatar, Doha 23874, Qatar (e-mail: milivoj.belic@qatar.tamu.edu).

Color versions of one or more of the figures in this paper are available online at http://ieeexplore.ieee.org.

Digital Object Identifier 10.1109/JSTQE.2019.2893762

I. Introduction

TERAHERTZ science has been steadily attracting a growing interest over the past decades. Lying above the upper limit of frequencies attainable in electronic devices and yet below frequencies at which light can be efficiently generated and detected, the current terahertz technology is faced with many challenges [1]. Among them, the development of fast electro-optic modulators for free-space terahertz signals, exhibiting low insertion loss and high modulation depth, has been gaining in importance over the past years considering the rapidly growing demands of wireless communications [2].

Following initial successful demonstrations of electro-optic modulation in terahertz [3], [4], the culprit of the very low modulation efficiency has been identified as the incompatibility of submillimeter wavelengths with much smaller features of the underlying electronic system [5]. A substantial increase in modulation efficiency has since been provided by various metallic structures [6], [7] whose resonant response translates into a stronger light-matter interaction helping bridge the two scales. Devices combining semiconductors (mainly gallium arsenide, GaAs) with metasurfaces have been of particular interest [8] as they offer high-speed modulation, a perspective of on-chip integration using established semiconductor technologies [9] and are fully compatible with quantum cascade lasers [1], the most promising source of terahertz radiation. Other material systems, such as liquid crystals [10]–[12] and graphene [13]–[15] more recently, have also been considered in depth, each presenting its own set of comparative advantages.

After the first prototype was introduced [6], a number of semiconductor-based terahertz metasurface modulators have been considered [7], [16]–[20] with widely ranging performance parameters. Perhaps the most convincing demonstration so far has been the double-channel heterostructure modulator [18] achieving modulation speed above 1 GHz and a modulation depth of 85%. Leaving important technical details aside, the above devices all derive their operation principle from the original work [6]. It involves a cut metal wire taking various shapes (e.g. a split-ring resonator or a dipole antenna) placed on top of a semiconductor, in which modulation occurs as a result of tuning the semiconductor conductivity beneath the gap, since a high conductivity effectively short-circuits the two parts.

Here we consider an alternative device concept whose main characteristic is that the tunable resonant element is buried
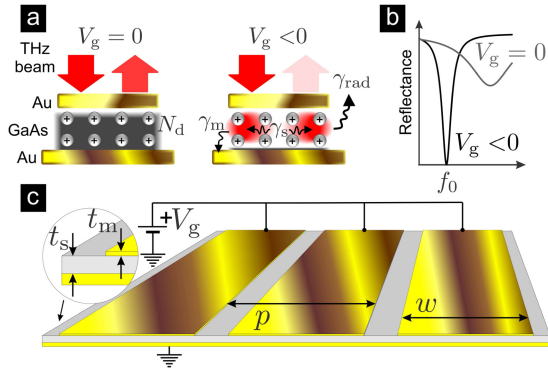
Fig. 1. (a) Operation principle, (b) Typical bias-dependent reflectance spectra, (c) A section of the device shown in real scale (in the actual device, the strips are repeated periodically). The epitaxial GaAs layer is selectively n-doped beneath the strips.

into the semiconductor akin to the one recently used in electrically tunable infrared polaritonic metasurfaces [21]. It comprises a metal-semiconductor-metal cavity of deeply subwavelength thickness known for providing a substantial light-matter interaction enhancement [22]. Such cavities have recently been employed in electrical control of intersubband polaritons [23], terahertz [24], [25] and infrared quantum detectors [26] and vertical-external-cavity surface-emitting quantum cascade lasers [27], [28]. In contrast to the listed examples which all rely on AlGaAs quantum heterostructures, the active region in our case is simply a single n-doped epitaxial layer of GaAs forming a Schottky contact at the interface with the top metal layer, allowing for tuning the n-GaAs permittivity by applying a gate voltage.

II. OPERATION PRINCIPLE AND DEVICE GEOMETRY

The basic element of the device is a metal-semiconductor-metal cavity array depicted in Fig. 1(a). A Schottky junction is formed between the top electrode (gate) and the epitaxial semiconductor layer while the contact to the bottom electrode (ground) is ohmic. The gold and GaAs combination of materials is considered because its optical properties in metal-semiconductor-metal cavities [29] as well as the relevant Schottky [30], [31] and ohmic contact [32] characteristics are well documented, however a range of other materials may suffice as well. At zero bias, the electron concentration n_e in each cavity (gray shading) is considered equal to the fully ionized donor concentration N_d (small spheres). If the doping is very high, so that the plasma oscillation frequency ω_p is above the incoming field frequency, the Drude response will be fast enough to screen the external fields out of the cavities and the device will act as a mirror. Upon applying a sufficiently large reverse voltage, the depletion layer of the Schottky junction extends over the entire cavity which now supports a photonic mode with eigenfrequency $\omega_0 = 2\pi f_0$ and is characterized by a radiative decay rate γ_{rad} and a non-radiative decay rate γ_0, the latter being the sum of the rate of photon absorption in the metal γ_m and semiconductor γ_s. If the geometrical parameters of the cavity

are chosen appropriately [11], the critical coupling condition

$$\gamma_{rad} = \gamma_0, \tag{1}$$

may be reached, ensuring the total absorption of an externally incident terahertz beam. Therefore, by switching V_g, a large reflectance modulation may be achieved in a band of frequencies around f_0, as depicted in Fig. 1(b).

In fact, the analysis below shows that efficient modulation does not strictly require a sub-plasma frequency operation ($\omega_p/\omega_0 > 1$), as long as the free carriers are able to blueshift ω_0 enough. Formally, one may analyze the eigenfrequency $\omega_0(V_g)$ and decay rates $\gamma_m(V_g)$, $\gamma_s(V_g)$, $\gamma_{rad}(V_g)$ as functions of V_g. However, since the quantitative connection between such a dependence and the modulation efficiency is not straightforward, here a direct approach is adopted whereby the decay rates are analyzed only for fully depleted cavities after which the modulation efficiency is evaluated without further reference to them.

For convenience, here the simplest implementation of the described concept is considered, as depicted in realistic scale in Fig. 1(c). The device represents a periodic array of long rectangular strips of width w and pitch p, connected to a common potential V_g at the far end. It is operative for one polarization (across the strips) only, but polarization-insensitive variants [11] can be straightforwardly devised by replacing the strips with symmetrical patches (e.g. circular or square-shaped). Invoking the temporal coupled-mode theory (TCMT) formalism [33], [34], the complex reflection coefficient of metal-semiconductor-metal cavity arrays with fundamental optical modes in the terahertz range [22] can, to an excellent approximation, be written as [35]

$$r(\omega) = \frac{\omega - \omega_0 + i(\gamma_0 - \gamma_{rad})}{\omega - \omega_0 + i(\gamma_0 + \gamma_{rad})}. \tag{2}$$

We use the TCMT formalism in conjunction with rigorous numerical simulations (see Appendix IV), whereby the three parameters ω_0, γ_0 and γ_{rad} are extracted by fitting Eq. (2) to the numerically calculated $r(\omega)$. While useful in providing a simple way of parametrizing the optical response of the device, the real advantage of the TCMT formalism stems from the fact that γ_0 and γ_{rad} are physically meaningful quantities which can be related to the cavity geometry and eigenmode field distribution, thus facilitating the design of cavities with desired $r(\omega)$.

The process of identifying a geometry which yields a critically coupled optical mode at a desired frequency f_0 can be illustrated on the example of $f_0 = 1$ THz. According to Fig. 1(c), it involves deciding on values of three geometrical parameters, w, p and t_s. Here the gold strip thickness t_m is set to 0.3 μm instead of being considered as a free parameter because its exact value is insignificant, as long as it is much smaller than the wavelength but large enough to ensure optical opacity. The cavity width w is determined from the target f_0 because the fundamental optical mode is a transverse-magnetic standing wave [22] whose eigenfrequency is only weakly affected by changing t_s and p (see Figs. 2(a,b) below). A slight lateral spill of the standing wave fields beyond the strip edges implies that the half-wavelength in the semiconductor $\lambda_{0,GaAs}/2$ is slightly larger than w.
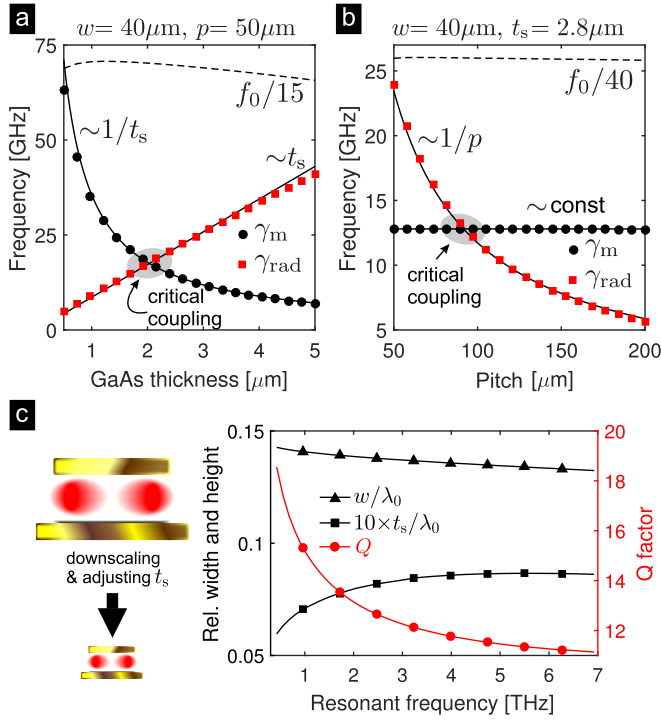
Fig. 2. TCMT parameters as a function of (a) semiconductor layer thickness, (b) pitch. (c) Geometrical parameters yielding critical coupling at full depletion (p is fixed at $1.25\,w$).

Assuming $n_{GaAs} = 3.3$ at 1 THz, yields $\lambda_{0,GaAs}/2 \approx 45.45\,\mu m$, starting from which we easily find $w = 40\,\mu m$ to yield $f_0 \approx 1$ THz.

To establish the role of GaAs thickness, in Fig. 2(a) we fix $p = 50\,\mu m$ and plot the TCMT parameters as a function of t_s. Since the cavity is assumed to be fully depleted, the absorption rate in the semiconductor layer γ_s will be negligible while γ_0 becomes equal to the metal absorption rate γ_m plotted in Fig. 2(a). The numerically calculated values of γ_m and γ_{rad}, represented by circles and squares respectively, are seen to fit very well to a t_s^{-1} and t_s curve (solid lines). The origin of the observed scaling of γ_m and γ_{rad} has been examined in Appendix C of [11] for the mathematically analogous case of circular patch cavities filled with a liquid crystal. This scaling follows from a straightforward consideration of how the modal fields are redistributed when the cavity height is changed, with the only subtlety being the eigenmode field normalization. Here we limit the discussion to noting that the observed trend is what one would expect: compressing the eigenmode into a thinner cavity causes the fields to penetrate more into the cladding on top and bottom, implying higher absorption in the metal and, therefore, the increase of γ_m with decreasing t_s. On the other hand, the radiation loss of a cavity must be proportional to the fraction of its surface not covered by metal and since the latter is proportional to t_s, we infer that γ_{rad} should decrease as t_s is decreased. In Fig. 2(a), adjusting t_s alone is found to be sufficient for achieving critical coupling, seen as the crossing of γ_m and γ_{rad} curves in Fig. 2(a). In fact, since two curves proportional to $\sim t_s^{-1}$ and $\sim t_s$ always have an intersection, we infer that adjusting t_s alone will be sufficient to fulfill Eq. (1) for any reasonable cavity. Meanwhile, the dashed

line depicting $f_0/15$ shows that f_0 undergoes only a small relative variation over the considered t_s interval, meaning that once t_s is fixed, w may be readjusted to set f_0 exactly to the desired value.

The effect of changing the pitch is considered in Fig. 2(b) where t_s is set to a representative value of $2.8\,\mu m$. For p below $50\,\mu m$, the strips spacing becomes too small, leading to the hybridization of adjacent cavity modes and their delocalization [29]. At the higher end, p is limited by the requirement that only the zeroth diffraction order is propagative. The calculated γ_m datapoints (circles) fit very well to the constant line. This follows from the fact that once adjacent cavities become sufficiently separated, the field of their eigenmodes becomes identical to the field of an isolated cavity. Since γ_m is determined by field penetration into the metal, it cannot depend on p. On the other hand, γ_{rad} is seen to decrease rapidly with p, which might appear surprising because it implies that the power emitted by each cavity is affected by p. This, however, is a natural consequence of the fact that the cavities represent an array of mutually coherent emitters. In Appendix IV we give a short proof that $\gamma_{rad} \sim p^{-1}$ approximately. This is confirmed in Fig. 2(b), with the $\sim p^{-1}$ fit (full line) matching the numerical data very well over the entire considered range of p. In this case, the dashed line representing $f_0/40$ shows that f_0 is virtually independent of p. Since γ_m remains invariant, there will be cases in which changing p alone will not be sufficient to reach critical coupling. For example, cavities with higher aspect ratios (t_s/w) will be highly overcoupled $\gamma_m \ll \gamma_{rad}$, so even at $p \approx \lambda_0$, γ_{rad} might still be substantially larger than γ_m. The reverse problem occurs with very small aspect ratios (highly undercoupled cavities), as in that case even for $p \approx w$, γ_{rad} might still be well below γ_m.

Now, consider a cavity with eigenfrequency ω_0 in which Eq. (1) is fulfilled for given t_s and p. If we decrease p, in order to retain critical coupling, we also have to decrease t_s. Since p does not affect it, γ_m is modified only because t_s was decreased, meaning that we end up with a cavity having both γ_m and γ_{rad} larger than in the initial cavity. Therefore, decreasing p increases the bandwidth $\Delta f = (\gamma_m + \gamma_{rad})/\pi$ of the device. A shorter p is also important as it allows smaller values for t_s, translating into lower operation voltage and higher speed. For these reasons, in what follows we set the pitch to $p = 1.25\,w$, (a value close to the onset of cavity mode hybridization) and adjust t_s until critical coupling is reached.

The above procedure may be repeated for an arbitrary frequency f_0. However, in order to find w and t_s that ensure critical coupling over the entire terahertz spectrum, it is more straightforward to employ geometrical scaling. Downscaling all geometrical parameters of a cavity array by a factor, upscales the TCMT parameters approximately by the same factor. However, small deviations from linear scaling due to material dispersion result in a cavity that does not meet the critical coupling condition exactly [35], meaning that t_s will have to be slightly adjusted to restore it. Figure 2(c) shows the values of w and t_s that yield critically coupled cavities, for resonant frequencies ranging from 0.3 THz up to 7 THz, beyond which GaAs cannot be used for this purpose, due to its optical phonons and onset of the reststrahlen band [29]. The plotted quantities are actually
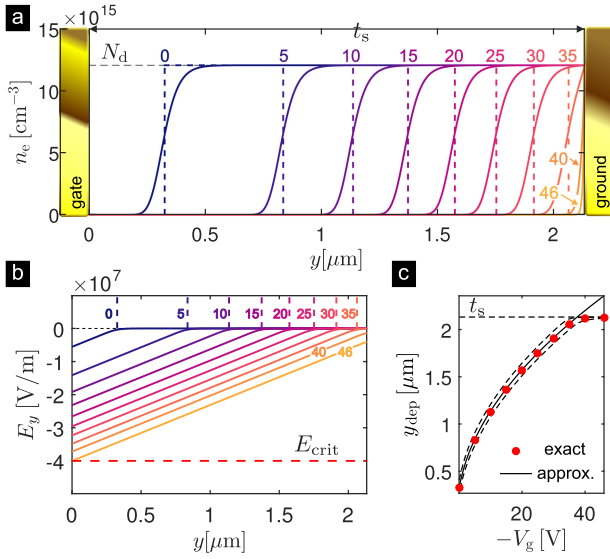
Fig. 3. Schottky junction under reverse bias showing the depletion layer reach-through effect. The profiles are drawn along the symmetry axis of a cavity with $p = 52.72\,\mu m$, $w = 42.18\,\mu m$, $t_s = 2.13\,\mu m$, $t_m = 0.3\,\mu m$ and $N_d = 1.2 \times 10^{16}\,cm^{-3}$, designed to operate at 1 THz. (a) Electron concentration (solid line - rigorous model, dashed - FDA) parametrized by $-V_g$, (b) Corresponding electric field profiles, (c) Depletion layer width with dashed lines indicating the transition width, defined as location where n_e reaches the $0.1\,N_d$ and $0.9\,N_d$ marks.

normalized to the free-space wavelength λ_0, demonstrating the mentioned deviation from the linear scaling law. For the same reason, the Q factor $Q = \omega_0/2(\gamma_m + \gamma_{rad}) = \omega_0/4\gamma_{rad}$ is seen to decrease slowly going towards higher frequencies.

III. DOPING CONCENTRATION AND PERFORMANCE ANALYSIS

A nonzero concentration $n_e(\mathbf{r})$ of free electrons in the cavity introduces a Drude term to the optical permittivity ε_{opt} of GaAs. The total permittivity becomes inhomogeneous and is given by [36], [37]

$$\varepsilon_s(\mathbf{r}, \omega) = \varepsilon_{opt}\left(1 - \frac{\omega_p^2(\mathbf{r})}{\omega(\omega + i\gamma_c)}\right), \qquad (3)$$

where the plasma frequency ω_p and intraband electron collision rate γ_c read

$$\omega_p(\mathbf{r}) = \sqrt{\frac{n_e(\mathbf{r})q^2}{\varepsilon_{opt}\varepsilon_0 m_c^*}}, \qquad \gamma_c = \frac{q}{\mu_n m_c^*}, \qquad (4)$$

while the realistic doping-dependent conduction band electron mobility μ_n is evaluated following [38]. At zero gate bias, $n_e \approx N_d$ in the entire cavity, except in a thin depletion layer beneath the gate. It is thus clear that the higher N_d is, the greater the voltage-induced change of permittivity will be, resulting in more effective modulation. The upper limit on N_d is set by the requirement that the cavity can be fully depleted before the avalanche breakdown of the Schottky junction.

To estimate the highest possible value of N_d, we consider the characteristic Schottky junction behavior under reverse bias illustrated in Fig. 3(a), where $n_e(\mathbf{r})$ is plotted along the vertical

axis going through the center of the cavity, with $-V_g$ as a parameter. The profiles drawn by solid lines are obtained using a rigorous solid-state physics framework based on a majority-carrier solution scheme (for details see Appendix B). For comparison, the step-like n_e profiles of the full depletion approximation (FDA) [39] are indicated by dashed lines. Apart from being abrupt, the FDA curves are a rather good match to the rigorous ones. This is demonstrated in Fig. 3(c) where the depletion layer width y_{dep}, defined as the distance from the junction at which n_e reaches $0.5\,N_d$, is drawn against $-V_g$ for both the rigorous (circular datapoints) and FDA model (solid line), the latter being given by

$$y_{dep} = \sqrt{\frac{2\varepsilon_{stat}\varepsilon_0(\psi_{bi} - V_g)}{qN_d}}, \qquad (5)$$

where $\psi_{bi} = 0.9\,V$ is the Schottky barrier height of the n-GaAs/Au interface, q the elementary charge and $\varepsilon_{stat} = 12.9$ the electrostatic dielectric permittivity of GaAs. With increasing reverse voltage, the depletion layer expands until it reaches the ground gold layer. In itself, the reach-through phenomenon is not associated with critical behavior [40], as a further increase of $-V_g$ merely causes a charge buildup on the gold side of the contact. To simplify the evaluation of the breakdown voltage, we employ the commonly-used critical field approximation [40], whereby the avalanche breakdown is assumed to occur once the electric field passes a critical value E_{crit}. The latter is dependent on the doping concentration, but for simplicity we take $E_{crit} = 4 \times 10^7\,V/m$ as a representative value [30] for the range of N_d considered in this work.

Neglecting the effect of strip edges, the only nonzero component of the static electric field is E_y and it reaches its highest value at the Schottky junction. According to FDA, $-E_{max} = qN_d y_{dep}/\varepsilon_{stat}\varepsilon_0$, from which we find the highest doping for $E_{max} = E_{crit}$ when $y_{dep} = t_s$

$$N_{d,max} = \frac{\varepsilon_{stat}\varepsilon_0 E_{crit}}{qt_s}. \qquad (6)$$

This value, however, is arrived at neglecting the tail of the actual n_e profile. To see this, note that in the Fig. 3 example, FDA predicts $-V_g = 37.48\,V$ as the reach-through voltage, while the actual n_e profiles in Fig. 3 show that even at $-V_g = 40\,V$, there is still a non-negligible concentration of electrons in the cavity. To reduce the remanent n_e at the ground contact, the cavity should be biased slightly above the reach-through voltage and to achieve this without avalanche breakdown, a slightly lower doping concentration is used, $N_d = 0.9 \times N_{d,max}$. The cavity shown in Fig. 3 has $t_s = 2.13\,\mu m$, giving $N_{d,max} = 1.34 \times 10^{16}\,cm^{-3}$, so the actual value used is $N_d = 1.2 \times 10^{16}\,cm^{-3}$. The numerically calculated electric field profiles $E_y(y)$ are shown in Fig. 3(b). On this scale, the latter virtually overlap with the field profiles predicted by FDA. From these, we find that the breakdown occurs around $-V_g \approx 46\,V$.

As a proof of concept, in Fig. 4 we analyze the switching of a device designed to operate at 1 THz. The first four panels, (a)–(d), depict $n_e(\mathbf{r})$, the normalized terahertz field magnitude $|\mathbf{E}(\mathbf{r})|/E_0$ excited by an incoming linearly polarized plane wave
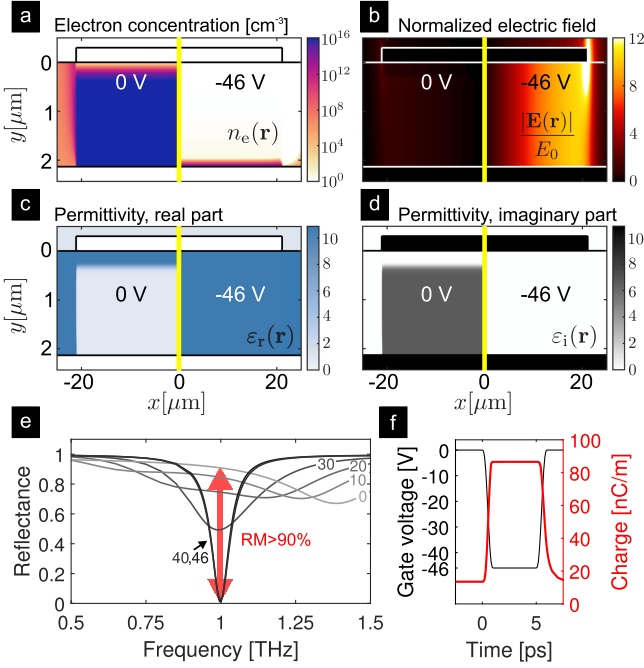
Fig. 4. Proof of concept simulation for the 1 THz device (for details, see Appendix IV and B). (a) Electron concentration, (b) High-frequency electric field distribution resulting from illumination at 1 THz, (c) Real and (d) imaginary part of permittivity at 1 THz. For better contrast, the range used in colormaps of panels (b)–(d) is saturated by cutting out the high electric field values at strip corners in (b), and gold permittivity values in (c) and (d). (e) Reflectance spectra parametrized by $-V_g$, (f) Transient response of the total charge in cavity to a 5 ps reverse bias pulse. (All the colormaps used in this article have been produced by a source code kindly provided by Peter Kovesi, see [41].)

with field amplitude E_0 falling perpendicularly onto the strip array, as well as the real $\varepsilon_r(\mathbf{r})$ and imaginary $\varepsilon_i(\mathbf{r})$ parts of $\varepsilon_s(\mathbf{r})$ given by Eq. (3). For conciseness in illustrating the switching effect of the gate voltage, we exploit the mirror symmetry of the problem. Noting that the calculated distributions exhibit this symmetry, in Figs. 4(a)–(d) we use the left half of the unit cell to plot the quantities calculated at $V_g = 0$ V while those corresponding to $V_g = -46$ V are shown in the right half.

The depleted cavity ($V_g = -46$ V) is seen to be virtually free of electrons, except at the bottom contact (note the logarithmic scale of the colormap). Consequently, ε_s is very close to ε_{opt} practically everywhere, thus justifying the assumptions made in designing the cavities in previous section. At the microscopic scale, the efficiency of the device is demonstrated by the huge difference in the electromagnetic field intensity evident from Fig. 4(b), where the field is seen to hardly penetrate the cavity at $V_g = 0$ V, while at $V_g = -46$ V the field enhancement in the cavity is around 10.

Figure 4(e) shows the calculated reflectance spectra $R(\omega) = |r(\omega)|^2$ parametrized by $-V_g$. At f_0 we have $R(\omega_0; 0\,\text{V}) \approx 90\%$ and $R(\omega_0; -46\,\text{V}) \approx 0\%$. Introducing the reflectance modulation (RM), and insertion loss (IL) as

$$\text{RM} = R(\omega_0; 0\,\text{V}) - R(\omega_0; V_{g,\min}),$$
$$\text{IL} = 1 - R(\omega_0; 0\,\text{V}), \tag{7}$$

with $V_{g,\min}$ denoting the avalanche breakdown voltage, we find RM and IL to be approximately 90% and 10%, respectively, which is excellent for solid-state terahertz modulators [5]. Since $R(\omega_0; V_{g,\min}) \approx 0\%$ by design, the proposed modulator will have a very high (theoretically infinite) extinction ratio which will in practice be limited by device fabrication tolerance. Previously considered Schottky junction based modulators [6], [7] used similar doping concentrations and, consequently, similar gate-induced permittivity changes. The origin of the increased modulation efficiency of the proposed device is the almost complete overlap of the resonant terahertz fields with the region in which ε_s is modified, which is known to be proportional to the change in resonant frequency and decay rates [42]. Finally, we note that the fact that the 40 V and 46 V reflectance curves almost overlap, indicates that the critical coupling effect is rather robust to the presence of the remanent electron concentration at the bottom electrode. It further implies that meeting the $\gamma_0 \approx \gamma_{rad}$ condition reasonably well should not be particularly difficult in practice, especially considering that various post-processing steps might also help [34].

Switching times in the subnanosecond range are among the key advantages of solid-state terahertz modulators over those based on liquid crystals, phase change or thermal tuning [8] where the switching time is in the millisecond range at best [11]. In recently demonstrated semiconductor-based terahertz modulators [16], [21] with ~10 MHz operating frequencies, the speed has been found to be limited not by the inherent response time of the device but by the driving circuit. More recently, however, modulation above 1 GHz has been demonstrated [18]. Therefore, with driving circuits being perfected, the inherent switching time of terahertz modulators might become the limiting factor.

An important aspect of the proposed device is its very high intrinsic speed, as a consequence of the ultrathin active region. This is demonstrated by numerical simulations of the cavity charge $Q(t)$ (per unit length along the strip axis) transient upon applying a rectangular pulse of reverse bias shown in Fig. 4(f). The $-V_g(t)$ pulse duration is set to 5 ps, with 0.5 ps 10%–90% rise and fall times. The corresponding rise time of $Q(t)$ is well below 1 ps, while the fall time is somewhat longer and calculated to be around 1 ps.

Such a short intrinsic response time originates from the very small distance t_s between the contacts, which is well below $\lambda_0/100$ as shown in Fig. 2(c). Here, as well as in [21], it is achieved by using a deeply-subwavelength cavity, while in [16], [18] the small distance between the electrodes is achieved at the expense of device complexity. Devices with laterally arranged contacts are likely to have a much longer intrinsic response time, increasing with the distance between the electrodes, as demonstrated in [43].

Having seen that the proposed device performs very well at $f_0 = 1$ THz, we now examine how changing f_0 affects the modulator performance. The above procedure for determining the appropriate donor concentration in conjuction with cavity parameters shown in Fig. 2(c) can be repeated to obtain the N_d values shown in Fig. 5(a). The corresponding inverse gate voltages required for full depletion are shown in panel (b), while
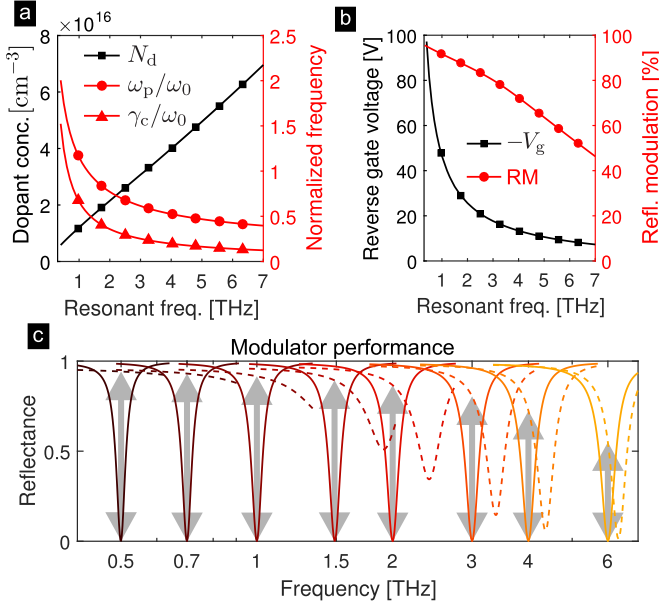
Fig. 5. Device parameters for operation across the terahertz spectrum, to be combined with geometrical parameters in Fig. 2(c). (a) Doping and normalized Drude parameters, (b) Gate voltage required for full cavity depletion and reflectance modulation. (c) Characteristic reflectance spectra for devices operating across the terahertz spectrum (solid line - biased, dashed line - no bias). The vertical gray arrows indicate the reflectance modulation.

the reflectance spectra for eight modulators with f_0 ranging over the terahertz spectrum are depicted in (c). In the latter, solid lines depict $R(\omega)$ in fully depleted state and the dashed lines the zero bias state. Note that the horizontal axis in Fig. 5(c) is shown in logarithmic scale, in order to better resolve all the depicted spectra. The thick vertical gray arrows indicate RM for each of the depicted modulators.

Extracting RM for spectra at various f_0, we obtain the curve in Fig. 5(b) showing the gradual decline of RM from more than 95% at 0.3 THz to around 46% at 7 THz. The reason for such behavior can be understood by noting that, because the electrostatic field at the junction must be less than E_{crit}, the surface density σ of the total charge in the cavity remains invariant with respect to f_0 and equals $N_d t_s$. This implies that as t_s is decreased, N_d and ω_p increase, but so that ω_p scales (roughly) as $\sim f_0^{1/2}$. Meanwhile, the modulation efficiency is determined by the change of permittivity in the cavity which can be effected by bias, which is equal to the Drude term contribution and proportional to ω_p/ω_0. The latter is drawn in Fig. 5(a) and, as expected, found to scale (roughly) as $\sim f_0^{-1/2}$.

Another feature arising at high f_0 is the change of the character of the cavity tuning. At 1 THz, the Drude contribution to ε_s has comparable real and imaginary parts, which is apparent in Fig. 4(c) and (d) and a consequence of the ratio γ_c/ω_0 being close to unity. Plotting this ratio in Fig. 5(a), we find that it also decreases at higher f_0, meaning that the voltage-induced change of permittivity becomes mainly real. The imaginary part of ε_s implies absorption in the semiconductor, introducing the semiconductor absorption term γ_s to the nonradiative decay rate. In terms of the reflectance spectra, this means that the cavity designed to be critically coupled at full depletion, is driven further

away from this condition at zero bias and has a significant amount of reflection at resonance (slightly shifted though). Such a behavior is nicely seen in the Fig. 4(e) plot. As f_0 approaches 7 THz, this changes significantly, as γ_s at zero bias remains rather small so the reflectance at cavity resonance remains close to zero, as seen in the $f_0 = 6$ THz modulator example in Fig. 5(c).

IV. SUMMARY

This article proposes a terahertz electro-optic modulator comprising an array of metal-semiconductor-metal cavities of deeply subwavelength thickness. The modulator operates by depleting the carriers from the doped semiconductor layer buried beneath a Schottky junction. Combining the extremely high terahertz field confinement with a reversely-biased Schottky junction in the reach-through regime, allows for a modulation performance that is predicted to match or even surpass existing devices. The proof of concept analysis presented for the modulator operating at 1 THz, based on a rigorous multiphysics framework incorporating Maxwell equations for terahertz waves and the drift-diffusion model describing carriers in the cavity, predicts an insertion loss around 10%, reflectance modulation of 90% and a theoretically infinite extinction ratio associated with cavities designed to work in the critically coupled regime. The performance is found to decrease in modulators designed to operate in the higher end of the terahertz spectrum, reaching insertion loss of 54% and reflectance modulation falling to 46% at 7 THz. This decline has been shown to be an inherent characteristic of the Drude response in which the plasma frequency scales as the square root of carrier concentration. In addition to forging strong light-matter interaction, the ultrathin cavity has been shown to allow for ultrafast intrinsic response times, which have been shown to be in the picosecond range.

APPENDIX A
LIGHT SCATTERING ANALYSIS

To obtain $r(\omega)$, the Maxwell equations are solved in frequency domain using the scattered field formulation with the background field $\mathbf{E}_b(\mathbf{r})$ being the sum of the incoming and the plane wave reflected from the opaque back metal electrode (normal incidence is assumed), and the scattered field $\mathbf{E}_s(\mathbf{r})$ being induced by the presence of the inhomogeneously doped semiconductor and the array of metal strips. The problem is represented by a two-dimensional model with a rectangular simulation domain, where the side boundaries are related with periodic conditions on $\mathbf{E}_s(\mathbf{r})$, while the air superstrate above the structure is represented by a few-wavelength-thick domain terminated by a perfectly matched layer. The solution at both the top and bottom boundaries is set by the zero-field (Dirichlet) boundary condition. $r(\omega)$ is obtained from $\mathbf{E}_s(\mathbf{r})$ as the complex coefficient of the zeroth diffraction order (the only propagating one in all considered cases).

The gold permittivity $\varepsilon_m(\omega)$ was assumed to have the Drude form

$$\varepsilon_m(\omega) = 1 - \frac{\omega_{p,Au}^2}{\omega(\omega + i\gamma_{c,Au})}, \tag{8}$$

with the gold plasma $\omega_p = 1.37 \times 10^{16}$ rad/s and collision frequency $\gamma_{c,Au} = 4.05 \times 10^{13}$ rad/s taken from [44].

The reasoning in the article relies on the concept of a leaky eigenmode whose interaction with the environment is quantified by its radiative γ_{rad} and non-radiative γ_0 decay rates. These may be introduced in an intuitive manner by assuming that both the dissipative effects (absorption in metal and semiconductor) and the coupling between the eigenmode and environment are weak enough to be treated perturbatively. In that case, the eigenmode energy U exhibits an exponential temporal decay with a decay rate equal to $\gamma_{rad} + \gamma_0$, whereby the total loss power $P_{loss} = P_{rad} + P_0$ is broken down into the radiation P_{rad} and absorption P_0 terms so that $\gamma_{rad} = P_{rad}/2U$ and $\gamma_0 = P_0/2U$. A deeper analysis employing TCMT [45] reveals a general connection between the decay rates of a weakly coupled resonant system and its scattering matrix [46] which, in case of a single-port system with one eigenmode, implies Eq. (2). For sufficiently high quality factors, the TCMT parameters are directly related to the complex eigenfrequency $\tilde{\omega} = \omega_0 + i\omega_I$ of the associated cavity quasi-normal mode [47], with $\omega_I = \gamma_0 + \gamma_{rad}$. As TCMT itself is not the focus of this work, the reader is referred to [35] and [11] for further details on the formalism in the current context.

To explain the dependence of γ_{rad} on p, let us assume that the cavity array eigenmode is excited and allowed to decay both radiatively and via absorption, and let $H(x) = H(x, y_0)$ denote the magnetic field phasor (only the z-component is nonzero) along a horizontal line $y = y_0$ chosen at an arbitrary height above the cavity array. Assuming the spacing between adjacent cavities is large enough, the total field $H(x)$ may be represented as a sum of fields emitted by individual cavities, $H(x) = \sum_{n=-\infty}^{\infty} H_{uc}(x - np)$, where $H_{uc}(x) = H_{uc}(x, y_0)$ is the magnetic field profile of an eigenmode of a single cavity centered at $x = 0$. Since $H(x)$ is periodic in x, it can be expanded into a Fourier series $H(x) = \sum_{m=-\infty}^{\infty} H^{(m)} \exp(im\Delta k)$ where $\Delta k = 2\pi/p$ and m is the diffraction order. The dependence of $H^{(m)}$ on p is seen after introducing the Fourier transform of the single-cavity field by $h_{uc}(k) = \int_{-\infty}^{\infty} H_{uc}(x) \exp(-ikx)dx$ and noting that $H^{(m)} = h_{uc}(m\Delta k)/p$, while $h_{uc}(m\Delta k)$ is obviously independent on p. In the considered spectral range, only the zeroth diffraction order is propagative so the radiated power flux through a unit cell equals $P_{uc,rad} = z_0 p|H^{(0)}|^2/2 = z_0|h_{uc}(0)|^2/2p$, with z_0 denoting the free-space impedance. Finally, denoting by U_{uc} the energy contained in one cavity, and by N the total number of cavities in the array (formally $N \to \infty$) we have

$$\gamma_{rad} = \frac{P_{rad}}{2U} = \frac{N P_{uc,rad}}{2N U_{uc}} = \frac{z_0|h_{uc}(0)|^2}{4U_{uc}} p^{-1}, \qquad (9)$$

thus proving the $\sim p^{-1}$ scaling stated in the article.

APPENDIX B
SOLID-STATE ANALYSIS

The gate bias effect on the carrier distribution is described using a rigorous solid-state physics framework based on a majority-carrier solution scheme, consisting in the conservation

TABLE I
SOLID-STATE PHYSICS PARAMETERS FOR GaAs [51]

Parameter	GaAs
Static permittivity, ε_{stat}	12.90
High-frequency permittivity, ε_{opt}	10.89
Effective electron mass, m_c^*/m_0	0.067
Energy band gap, E_g (eV)	1.424
Electron affinity, χ_0 (eV)	4.07
Conduction band density of states, N_c (cm^{-3})	4.7×10^{17}
Valence band density of states, N_v (cm^{-3})	9.0×10^{18}

law for charge (Poisson equation) and the time-dependent current continuity equations [48], [49]. The current density is expressed by the drift-diffusion expressions, while the simplified Maxwell-Boltzmann energy distribution is used for the carrier concentration, allowed by the moderate doping level of the n-GaAs cavity. The Schottky contact is described as a source/sink for carriers, treated as a surface recombination mechanism [50]. The Schottky barrier height of the n-GaAs/Au interface is considered 0.9 V, while the effective Richardson's constant for the n-doped GaAs is set equal to 4.4 Acm^{-2}K^{-2} [39]. The lateral intrinsic GaAs sections are interfaced to the central n-GaAs (under the strips) using quasi-Fermi level continuity boundary conditions. The resulting system of partial differential equations is set to additionally satisfy insulating conditions at the external metamaterial unit-cell boundaries and the thermodynamic equilibrium at the back contact, considered ideal ohmic. It is highlighted that, even though both contacts can be indiscriminately represented as Au layers from an electromagnetic standpoint, suitable Au-based alloys should be used in practice to ensure ohmic conditions at the back contact [32], having, though, marginal effect on the electromagnetic analysis.

The GaAs semiconductor parameters are listed in Table I, while the carrier mobility is calculated using [38]. The Au work-function is set equal to 5.1 eV.

REFERENCES

[1] M. Tonouchi, "Cutting-edge terahertz technology," *Nature Photon.*, vol. 1, pp. 97–105, 2007.
[2] D. M. Mittleman, "Perspective: Terahertz science and technology," *J. Appl. Phys.*, vol. 122, no. 23, 2017, Art. no. 230901.
[3] R. Kersting, G. Strasser, and K. Unterrainer, "Terahertz phase modulator," *Electron. Lett.*, vol. 36, no. 13, pp. 1156–1158, Jun. 2000.
[4] T. Kleine-Ostmann, P. Dawson, K. Pierz, G. Hein, and M. Koch, "Room-temperature operation of an electrically driven terahertz modulator," *Appl. Phys. Lett.*, vol. 84, no. 18, pp. 3555–3557, 2004.
[5] R. Degl'Innocenti, S. J. Kindness, H. E. Beere, and D. A. Ritchie, "All-integrated terahertz modulators," *Nanophotonics*, vol. 7, pp. 127–144, 2018.
[6] H.-T. Chen *et al.*, "Active terahertz metamaterial devices," *Nature*, vol. 444, pp. 597–600, 2006.
[7] H.-T. Chen *et al.*, "A metamaterial solid-state terahertz phase modulator," *Nature Photon.*, vol. 3, pp. 148–151, 2009.
[8] M. Rahm, J.-S. Li, and W. J. Padilla, "THz wave modulators: A brief review on different modulation techniques," *J. Infrared Millimeter Terahertz Waves*, vol. 34, no. 1, pp. 1–27, 2013.

[9] J. Yoon *et al.*, "GaAs photovoltaics and optoelectronics using releasable multilayer epitaxial assemblies," *Nature*, vol. 465, pp. 329–334, 2010.

[10] D. Shrekenhamer, W.-C. Chen, and W. J. Padilla, "Liquid crystal tunable metamaterial absorber," *Phys. Rev. Lett.*, vol. 110, Apr. 2013, Art. no. 177403.

[11] G. Isić, B. Vasić, D. C. Zografopoulos, R. Beccherelli, and R. Gajić, "Electrically tunable critically coupled terahertz metamaterial absorber based on nematic liquid crystals," *Phys. Rev. Appl.*, vol. 3, Jun. 2015, Art. no. 064007.

[12] B. Vasić, D. C. Zografopoulos, G. Isić, R. Beccherelli, and R. Gajić, "Electrically tunable terahertz polarization converter based on overcoupled metal-isolator-metal metamaterials infiltrated with liquid crystals," *Nanotechnology*, vol. 28, no. 12, 2017, Art. no. 124002.

[13] B. Sensale-Rodriguez *et al.*, "Extraordinary control of terahertz beam reflectance in graphene electro-absorption modulators," *Nano Lett.*, vol. 12, no. 9, pp. 4518–4522, 2012.

[14] W. Gao *et al.*, "High-contrast terahertz wave modulation by gated graphene enhanced by extraordinary transmission through ring apertures," *Nano Lett.*, vol. 14, no. 3, pp. 1242–1248, 2014.

[15] S.-F. Shi *et al.*, "Optimizing broadband terahertz modulation with hybrid graphene/metasurface structures," *Nano Lett.*, vol. 15, no. 1, pp. 372–377, 2015.

[16] D. Shrekenhamer *et al.*, "High speed terahertz modulation from metamaterials with embedded high electron mobility transistors," *Opt. Express*, vol. 19, no. 10, pp. 9968–9975, May 2011.

[17] N. Karl *et al.*, "An electrically driven terahertz metamaterial diffractive modulator with more than 20 dB of dynamic range," *Appl. Phys. Lett.*, vol. 104, no. 9, 2014, Art. no. 091115.

[18] Y. Zhang *et al.*, "Gbps terahertz external modulator based on a composite metamaterial with a double-channel heterostructure," *Nano Lett.*, vol. 15, no. 5, pp. 3501–3506, 2015.

[19] M. T. Nouman *et al.*, "Terahertz modulator based on metamaterials integrated with metal-semiconductor-metal varactors," *Sci. Rep.*, vol. 6, 2016, Art. no. 26452.

[20] Z. Zhou, S. Wang, Y. Yu, Y. Chen, and L. Feng, "High performance metamaterials-high electron mobility transistors integrated terahertz modulator," *Opt. Express*, vol. 25, no. 15, pp. 17832–17840, Jul. 2017.

[21] J. Lee *et al.*, "Ultrafast electrically tunable polaritonic metasurfaces," *Adv. Opt. Mater.*, vol. 2, no. 11, pp. 1057–1063, 2014.

[22] Y. Todorov *et al.*, "Strong light-matter coupling in subwavelength metal-dielectric microcavities at terahertz frequencies," *Phys. Rev. Lett.*, vol. 102, May 2009, Art. no. 186402.

[23] A. A. Anappara, A. Tredicucci, G. Biasiol, and L. Sorba, "Electrical control of polariton coupling in intersubband microcavities," *Appl. Phys. Lett.*, vol. 87, no. 5, 2005, Art. no. 051105.

[24] A. Benz *et al.*, "Resonant metamaterial detectors based on THz quantum-cascade structures," *Sci. Rep.*, vol. 4, 2014, Art. no. 4269.

[25] D. Palaferri *et al.*, "Patch antenna terahertz photodetectors," *Appl. Phys. Lett.*, vol. 106, no. 16, 2015, Art. no. 161102.

[26] D. Palaferri *et al.*, "Ultra-subwavelength resonators for high temperature high performance quantum detectors," *New J. Phys.*, vol. 18, no. 11, 2016, Art. no. 113016.

[27] L. Xu *et al.*, "Terahertz metasurface quantum-cascade VECSELs: Theory and performance," *IEEE J. Sel. Topics Quantum Electron.*, vol. 23, no. 6, pp. 1–12, Nov. 2017.

[28] L. Xu *et al.*, "Metasurface quantum-cascade laser with electrically switchable polarization," *Optica*, vol. 4, no. 4, pp. 468–475, Apr. 2017.

[29] Y. Todorov *et al.*, "Optical properties of metal-dielectric-metal microcavities in the THz frequency range," *Opt. Express*, vol. 18, no. 13, pp. 13886–13907, Jun. 2010.

[30] B. J. Baliga, R. Ehle, J. R. Shealy, and W. Garwacki, "Breakdown characteristics of gallium arsenide," *IEEE Electron Device Lett.*, vol. EDL-2, no. 11, pp. 302–304, Nov. 1981.

[31] M. Hudait and S. Krupanidhi, "Breakdown characteristics of MOVPE grown Si-doped GaAs Schottky diodes," *Solid-State Electron.*, vol. 43, no. 12, pp. 2135–2139, 1999.

[32] A. Baca, F. Ren, J. Zolper, R. Briggs, and S. Pearton, "A survey of ohmic contacts to III-V compound semiconductors," *Thin Solid Films*, vol. 308/309, pp. 599–606, 1997.

[33] S. Fan, W. Suh, and J. D. Joannopoulos, "Temporal coupled-mode theory for the Fano resonance in optical resonators," *J. Opt. Soc. Amer. A*, vol. 20, no. 3, pp. 569–572, Mar. 2003.

[34] J.-M. Manceau, S. Zanotto, I. Sagnes, G. Beaudoin, and R. Colombelli, "Optical critical coupling into highly confining metal-insulator-metal resonators," *Appl. Phys. Lett.*, vol. 103, no. 9, 2013, Art. no. 091110.

[35] G. Isić, and R. Gajić, "Geometrical scaling and modal decay rates in periodic arrays of deeply subwavelength terahertz resonators," *J. Appl. Phys.*, vol. 116, no. 23, 2014, Art. no. 233103.

[36] R. Ulbricht, E. Hendry, J. Shan, T. F. Heinz, and M. Bonn, "Carrier dynamics in semiconductors studied with time-resolved terahertz spectroscopy," *Rev. Mod. Phys.*, vol. 83, pp. 543–586, Jun. 2011.

[37] D. Lockwood, G. Yu, and N. Rowell, "Optical phonon frequencies and damping in AlAs, GaP, GaAs, InP, InAs and InSb studied by oblique incidence infrared spectroscopy," *Solid State Commun.*, vol. 136, no. 7, pp. 404–409, 2005.

[38] M. Sotoodeh, A. H. Khalid, and A. A. Rezazadeh, "Empirical low-field mobility model for III-V compounds applicable in device simulation codes," *J. Appl. Phys.*, vol. 87, no. 6, pp. 2890–2900, 2000.

[39] S. Sze and K. N. Kwok, *Physics of Semiconductor Devices*. Hoboken, NJ, USA: Wiley, 2007.

[40] C. Bulucea, "Breakdown voltage of diffused epitaxial junctions," *Solid State Electron.*, vol. 34, no. 12, pp. 1313–1318, 1991.

[41] P. Kovesi, "Good colour maps: How to design them," 2015, arXiv/1509.03700.

[42] G. Isić, R. Gajić, and S. Vuković, "Plasmonic lifetimes and propagation lengths in metallodielectric superlattices," *Phys. Rev. B*, vol. 89, Apr. 2014, Art. no. 165427.

[43] H.-T. Chen *et al.*, "Hybrid metamaterials enable fast electrical modulation of freely propagating terahertz waves," *Appl. Phys. Lett.*, vol. 93, no. 9, 2008, Art. no. 091117.

[44] M. A. Ordal, R. J. Bell, R. W. Alexander, L. L. Long, and M. R. Querry, "Optical properties of fourteen metals in the infrared and far infrared: Al, Co, Cu, Au, Fe, Pb, Mo, Ni, Pd, Pt, Ag, Ti, V, and W," *Appl. Opt.*, vol. 24, no. 24, pp. 4493–4499, Dec. 1985.

[45] H. A. Haus and W. Huang, "Coupled-mode theory," *Proc. IEEE*, vol. 79, no. 10, pp. 1505–1518, Oct. 1991.

[46] W. Suh, Z. Wang, and S. Fan, "Temporal coupled-mode theory and the presence of non-orthogonal modes in lossless multimode cavities," *IEEE J. Quantum Electron.*, vol. 40, no. 10, pp. 1511–1518, Oct. 2004.

[47] P. Lalanne, W. Yan, K. Vynck, C. Sauvan, and J.-P. Hugonin, "Light interaction with photonic and plasmonic resonances," *Laser Photon. Rev.*, vol. 12, no. 5, 2018, Art. no. 1700113.

[48] G. Sinatkas, A. Pitilakis, D. C. Zografopoulos, R. Beccherelli, and E. E. Kriezis, "Transparent conducting oxide electro-optic modulators on silicon platforms: A comprehensive study based on the drift-diffusion semiconductor model," *J. Appl. Phys.*, vol. 121, no. 2, 2017, Art. no. 023109.

[49] G. Sinatkas and E. E. Kriezis, "Silicon-photonic electro-optic phase modulators integrating transparent conducting oxides," *IEEE J. Quantum. Electron.*, vol. 54, no. 4, pp. 1–8, Aug. 2018.

[50] C. Crowell and S. Sze, "Current transport in metal-semiconductor barriers," *Solid State Electron.*, vol. 9, no. 11, pp. 1035–1048, 1966.

[51] V. Agranovich and Y. Gartstein, "Gallium arsenide (GaAs)," in *Handbook Series on Semiconductor Parameters*, vol. 1, M. Levinshtein, S. Rumyantsev, and M. Shur, Eds. Singapore: World Scientific, 2000.

Authors' photographs and biographies not available at the time of publication.